Numerical modelling of electrochemical deposition techniques for healing concrete damaged by alkali silica reaction

Qing-feng Liu[a,b,*], Zhaozheng Meng[a,b], Dongshuai Hou[c], Yu Zhou[a,b], Yuxin Cai[a,b],

Mingzhong Zhang[d], Vivian W.Y.Tam[e]

[a] State Key Laboratory of Ocean Engineering, School of Naval Architecture, Ocean and Civil Engineering, Shanghai Jiao Tong University, Shanghai, China

[b] Shanghai Key Laboratory for Digital Maintenance of Buildings and Infrastructure, Shanghai, China

[c] Department of Civil Engineering, Qingdao University of Technology, Qingdao, China

[d] Department of Civil, Environmental and Geomatic Engineering, University College London, London, WC1E 6BT, UK

[e] School of Engineering, Design and Built Environment, Western Sydney University, NSW, 2751, Australia

[*] Corresponding Author, *Email address: liuqf@sjtu.edu.cn(Q.-F. Liu)*

Abstract: Alkali silica reaction (ASR) is a long-term factor that causes concrete cracking, and the ingress of harmful agents such as chloride can then be promoted by the ASR-induced cracks. Electrochemical deposition method (EDM) is a promising nondestructive rehabilitation technique which has two-fold advantages of crack repair and chloride removal. In this study, the entire process from ASR-induced cracking for crack repair by EDM is studied for the first time by coupling three sub-models involving different disciplines: (1) multi-ionic transport model, (2) ASR cracking model; and (3) crack repair model. The consumptions and interactions among various ionic species during ASR and electrochemical deposition are quantitively reflected in multi-ionic transport model. The ASR cracking model is developed considering the local mechanical variances of concrete composites. The crack repair model can successfully visualize the crack closure status, and the time-dependent porosity and diffusion coefficients during the treatment have also been well reflected. The proposed model is calibrated and validated against experimental data to ensure the prediction accuracy. A subsequent parameter shows that increase in alkali silica aggregates volume fraction can facilitate cracking process. Besides, for electrochemical deposition treatment on ASR-induced cracks, setting all exposed surfaces as anode can effectively improve the repair rate, and adoption of pulse current can ensure the continuous supply of magnesium ions from external anolyte. Other findings which have not been reported in existing studies are also highlighted, which is hoped to better guide the application in practical engineering.

Keywords: Electrochemical rehabilitation; ASR; Multi-ionic transport; Cracking; Crack healing; Numerical modelling

1. Introduction

Alkali Silica Reaction (ASR) has been regarded as one of the most serious long-term deterioration factors for RC structures [1-3]. It has been characterized as the chemical reactions between alkali reactive silica in aggregates and alkali ions in concrete pore solutions [4-6]. The subsequent product, expansive ASR gel, can lead to the internal stress development, cracking, and even spalling of concrete cover [7-9]. The cracks induced by ASR will then reduce the carrying capacity of existing concrete structures [10, 11], and will also provide convenient channels for the ingress of harmful ions like chloride into concrete, causing a series of concrete durability damages [12, 13]. Consequently, crack repair and healing techniques for cementitious material are essential for prolonging the service life of RC structures.

Various crack repair methods including epoxy injection, grouting and self-healing materials have been proposed and proved to be effective ways for crack closure [14-16]. However, the abovementioned methods can only repair concrete in the cracked area, while fail to prevent sound part from further damage [17]. Besides, their inconveniences on hydraulic structures like dams and marine structures where ASR typically occur also limit the wider application. Electrochemical Deposition Method (EDM) is a promising nondestructive crack repair technique, which has been favored due to the convenience for marine and hydraulic structures where other methods are either costly or inappropriate [18, 19]. By making the embedded rebar as the cathode and the external titanium mesh as the anode, and applying current between the cathode and anode, metal cations (Zn^{2+} or Mg^{2+}) in the external anolyte will migrate into the

damaged concrete, and react with hydroxyl ions in the alkaline concrete pore solution to produce depositions (ZnO or Mg(OH)$_2$) filling exposed cracks [20]. Moreover, harmful ionic species like chloride can also be extracted from concrete to reduce the potential corrosion risk of steel reinforcements [21, 22]. Depositions formed in pore solutions can also improve the compactness and impermeability of concrete and further prevent the ingress of harmful agents in the external environment [23].

The entire process from ASR-induced cracking to crack repair by EDM includes three subprocesses: ionic transport governed by diffusion and migration, ASR-induced cracking and crack repair through electrochemical deposition. It should be noted that these three subprocesses are internally coupled and interactive during the life-cycle process of RC structures. Therefore, in order to study and predict such a complicated process with a large time span, it is necessary to analyze each subprocess and then build logical connections to construct a comprehensive numerical model.

Firstly, multi-ionic transport process runs through the whole process from alkali silica reaction to electrochemical deposition, so a deep understanding on this subprocess is the basis of the modelling work. Numerous studies have focused on the multi-ionic transport process in porous medium like concrete [24-27]. Liu et al. [28] studied the multi-ionic transport behavior in cracked concrete with the multi-component model, and the results indicated that the interactions among various ions are crucial to the ionic profile distributions. Yang et al. [29] investigated the migration process of multi-ionic species with concentration-dependent diffusion coefficients, and it showed the time-dependent boundary conditions on anode and cathode surface should

be carefully considered to obtain acceptable predictive results. Recently, Mao et al. [30] numerically modelled the ASR mitigation process with the coupling of lithium and chloride migration, but the consumptions and chemical reactions among various ionic species have not been explicitly explained. Therefore, considering chemical reactions including ASR and deposition generation, as well as the electrochemical reactions on the electrode surface, the ionic consumptions and interactions should be quantitively reflected to better depict the ionic transport behavior in concrete.

As for the ASR-induced cracking process, Dunant et al., have reported that the standard continuum methods may fail to precisely capture the actual degradation of ASR affected concrete [31], so discrete cracking method has been favored due to its advantages in considering the interface strengths in heterogeneous materials [32-34]. Wang et al. [35, 36] have modelled the concrete cracking process under the coupled effect of ASR and delayed ettringite formation. Rezakhani et al. [4] built a multiscale framework based on the Lattice Discrete Particle Model (LDPM). Miura et al. [37] studied the effect of expansive sites of ASR gel on crack distribution patterns by the three-dimensional Rigid Body Spring Model (3D RBSM), and they concluded that aggregates should be modelled with true grading and distribution to realistically predict the crack propagation process. In addition to discrete method, Pan et al. carried out a series of numerical studies on the cracking behavior of ASR affected concrete dams by concrete damage plasticity model [38, 39]. Giorlar et al. extended Dunant's model [40] to study the combined effect of creep and ASR, and they found that the ASR expansion rate mainly depended on the amount expansive gel rather than formation rate [41].

Multon et al. [42] studied the cracking caused by internal expansion of concrete by smeared cracking method, and they pointed out the geometrical shape of internal expansion phases (e.g., alkali reactive aggregates) would impact the direction of crack propagation. Therefore, the morphology of aggregates where ASR occurs should be carefully treated to reflect the crack distribution patterns more realistically. It should also be noted that only limited studies have coupled the alkali silica reactions into mechanical cracking, so the chemical kinetics of alkali silica reactions and the relationships with the internal volumetric expansion still need more attentions.

As for the crack repair by electrochemical deposition method, many scholars have studied this subject area by experimental approach. Otsuki and Ryu et al. [18, 43] carried out experiments on repairing shrinkage cracks and corrosion-induced cracks by electrochemical deposition method. Then, Nishida et al. [44] investigated the selection of cation types in external anolyte, and they found that both magnesium and zinc ions possessed excellent repair effect. Recently, Chu et al. [45-47] conducted a series experimental researches on the influencing factors of electrochemical deposition method on load-induced cracks, and they reported that in addition to the magnitude of the current density, the frequency of the current also influenced the crack closure rate. Nevertheless, compared with the existing large number of experimental studies, only a few researches have focused on numerical ones. Chen et al. [48, 49] built micro-mechanical models to predict the mechanical behavior after electrochemical deposition treatment. Zhou et al. [50] built a numerical model with the coupling of ionic transport and electrochemical deposition. However, the concrete was treated as a homogeneous

material, and the fracture was artificially generated with no tortuosity which could result to overestimation of crack closure rates. Therefore, numerical model taking into account of the inherent heterogeneity of concrete composite, and the influence of crack distribution patterns, particularly for ASR-induced cracks, should be built.

According to the literature review mentioned above, although previous studies have made great contributions to this field, knowledge gaps still exist and can be concluded as follows. Currently, there is no numerical models available for predicting the entire process from ASR cracking to crack repairing by electrochemical deposition method. The interconnections among these three complexly coupled subprocesses still need to be clarified to better understand the underlying mechanisms. In addition, improvements can also be made in the research of subprocesses. Firstly, traditional ionic transport model which cannot consider the ionic consumptions and chemical reactions may fail to accurately depict the interactions among multiple ionic species. The ionic flux on electrode surface caused by electrochemical reactions should also be quantitively reflected. Secondly, although fracture mechanics on ASR have obtained increasingly more attention, volumetric expansion of ASR gel are commonly based on linear expansion which is not consistent with actual observation. Besides, most previous models were based on the assumption of circular aggregates [36, 37, 51], which will ignore the anisotropy of crack distribution patterns to some extent. Finally, it should be noted that limited numerical models have been built to study the crack repair process. Compared with experimental approaches, numerical models have the strength in providing better visualization on crack closure statue and ionic concentration profiles

more efficiently and cost-effectively. Therefore, building numerical models which can reproduce the entire process including concrete failure and rehabilitation is of great significance for revealing mechanisms, and also providing guidance to practical engineering.

Considering the abovementioned knowledge gaps, three advanced sub-models (i.e., multi-ionic transport model, ASR cracking model and crack repair model) have been correspondingly proposed and coupled together for the first time. In multi-ionic transport model, the consumptions of metal cations and hydroxyl ions during deposition reactions, and the electrochemical reactions on the cathode and anode surfaces will be quantitively considered. Moreover, the interactions among various ions species in the concrete pore solution will also be quantified in the proposed multi-ionic transport model. In addition to reactions in pore solution, alkali silica reactions in aggregates will also be modelled to calculate the volumetric expansion of alkali active aggregates. Then, in the cracking model, the weak mechanical property of interfacial transition zone (ITZ) between aggregates and cement has also been taken into account to calculate the ASR-induced crack distribution patterns in mesoscopic level. Damage index like total crack length and crack area will also be quantitively discussed. In the case of crack repair model, the formation process of depositions in both crack area and concrete pore solutions can be successfully visualized. The influence of depositions on ionic transport is also characterized by the time-dependent ionic diffusion coefficients. Finally, the three sub-models are verified by experimental data and coupled together to predict the entire process from ASR-induced cracking to crack repairing. Potential influence

factors like volume fraction of alkali active aggregates, current frequency and density, and anode electrode position will be investigated through a detailed parametric analysis, which is hoped to better guide the actual application of electrochemical deposition method.

2. Model foundations

As mentioned previously, three internally coupled process should be modelled in order to comprehensively study the entire process from ASR cracking to crack repair by electrochemical deposition method. The relationships among the sub-models presented in this work is shown in Fig.1. The multi-ionic transport model, as shown in Fig.1(a), interacts both with ASR cracking model and crack repair model. For the ASR cracking which is governed by the ionic diffusion, the alkali silica reactions will initiate with the ingress of alkali ions into alkali reactive aggregates. The subsequently generated expansive gel will exert internal stress and finally result to cracking of concrete cover, as shown in Fig.1(b). For the crack repair which is mainly governed by ionic migration under the effect of externally applied electric field, the cation ions in the in external anode solution will migrate into the cracked concrete and react with hydroxyl ions to precipitate depositions filling the previously exposed cracks, as shown in Fig.1(c). On the other hand, chemical reactions are involved in both ASR cracking model and crack repair model, which will in turn impact the ionic distribution profiles calculated by multi-ionic transport model. Therefore, analyzing subprocesses with the consideration of interactions forms the basis of establishing the coupled model.
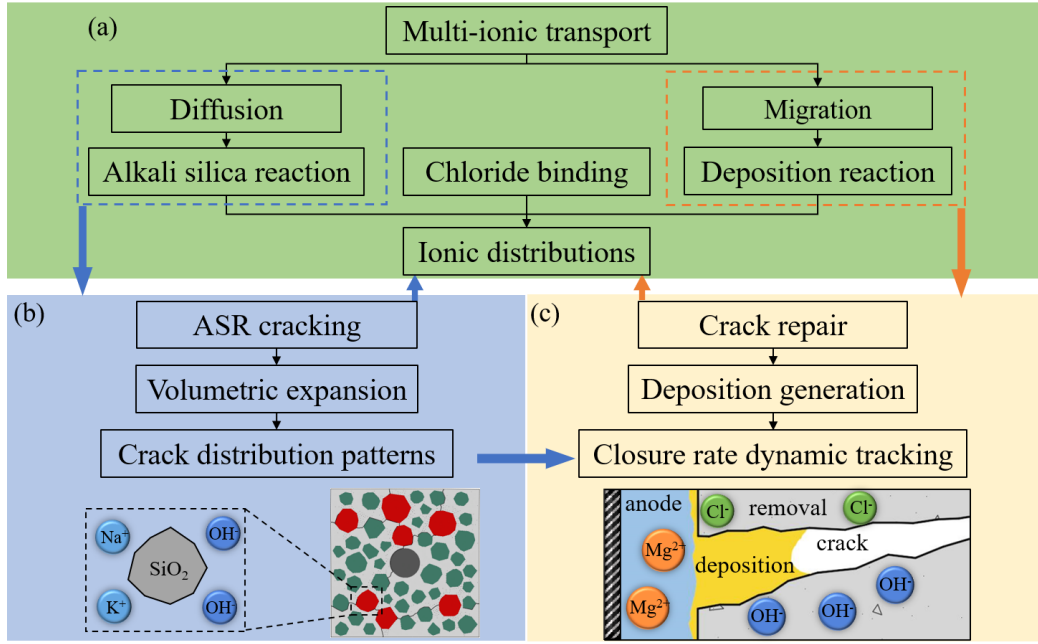
Fig.1 Schematic diagram of the internal relationships of the three sub-models.

2.1 Multi-ionic transport model

As mentioned previously, both alkali silica reaction and crack repair rely on the multi-ionic transport process, so the modelling work on multi-ionic transport behavior will be firstly discussed. In a completely saturated concrete pore solution, the ionic transport behavior can be depicted by the Nernst-Planck equation as:

$$J_k = \underbrace{-D_k \nabla C_k}_{\text{diffusion}} \underbrace{-D_k C_k \left(F Z_k / RT \right) \nabla U}_{\text{migration}} \quad (k = 1, 2, ..., n) \tag{1}$$

where the first term on the right side of the equation depicts the diffusion caused by concentration difference; the second term on the right side of the equation depicts the migration caused by potential difference; subscript k represents the k-th ionic species in the concrete pore solution; J_k is the ionic flux during transport; D_k, C_k and Z_k represent the diffusion coefficient, ionic concentration and charge number of the k-th ion respectively; F, R and T represent the Faraday constant (9.648×10^{-4} C·mol^{-1}), ideal gas constant (8.314 J·mol^{-1}K^{-1}) and absolute temperature (298.15 K) respectively; U

1   represents the electrostatic potential.

2   Considering the ionic consumptions in alkali silica reaction and electrochemical

3   deposition, the mass conservation used in traditional ionic transport model is no longer

4   suitable and should be modified with the sink or reactive term, S_k, which can be

5   expressed as:

6    $$\frac{\partial C_k}{\partial t} = -\nabla J_k + S_k \tag{2}$$

7   where reactive term S_k is used to quantify the ionic consumptions in alkali silica reaction

8   and deposition reaction, which will be discussed in the next two Sections. Substituting

9   Eq. (1) into Eq. (2), the change of ionic concentrations with time can be given by the

10   following equation.

11   $$\frac{\partial C_k}{\partial t} = \underbrace{D_k \nabla^2 C_k}_{\text{diffusion}} + \underbrace{\nabla\left[D_k Z_k C_k \left(F/RT\right)\nabla U\right]}_{\text{migration}} + \underbrace{S_k}_{\text{reaction}} \quad (k=1,2,...,n) \tag{3}$$

12   In addition to ionic consumptions caused by chemical reactions, free chloride ion

13   in concrete composite can be adsorbed by cementitious materials to form bound

14   chloride, which is called chloride binding effect. Here, the widely adopted Langmuir

15   isotherm is used to characterize the relations between free chloride concentration C_{Cl^-}

16   and bound chloride concentration B_{Cl^-} [52], which can be depicted as:

17   $$B_{Cl^-} = \frac{\alpha C_{Cl^-}}{w\left(1 + \beta C_{Cl^-}\right)} \tag{4}$$

18   where α and β are fitting parameters which is taken as 0.42 and 0.8×10^{-3} $m^3 \cdot mol^{-1}$; w is

19   the water content in unit weight of cement which is taken as 0.3 according literature

20   [53]. The transport equation for chloride should also be revised as:

1
$$\frac{\partial C_{Cl^-}}{\partial t} + \frac{\partial B_{Cl^-}}{\partial t} = D_{Cl^-}\nabla^2 C_{Cl^-} + \nabla\left[D_{Cl^-}Z_{Cl^-}C_{Cl^-}\left(F/RT\right)\nabla U\right] \tag{5}$$

2　substituting Eq. (4) into Eq. (5), the following transport equation for chloride ion can

3　be obtained as:

4
$$\left(1+\xi\right)\frac{\partial C_{Cl^-}}{\partial t} = D_{Cl^-}\nabla^2 C_{Cl^-} + \nabla\left[D_{Cl^-}Z_{Cl^-}C_{Cl^-}\left(F/RT\right)\nabla U\right] \tag{6}$$

5　where ξ equals $\frac{\alpha}{w(1+\beta C_{Cl^-})^2}$.

6　　Besides, the current conservation should also be taken into account to ensure the

7　ionic flow in concrete pore solution comply with the externally applied current density,

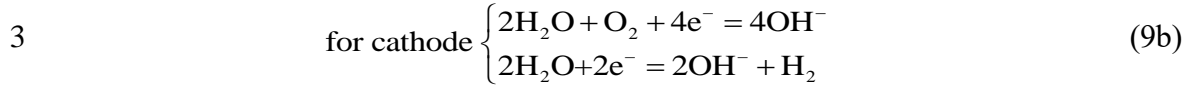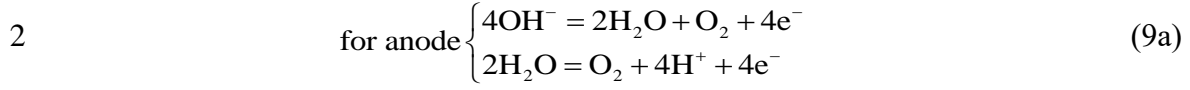8　which can be given by

9
$$i = F\sum_{k=1}^{n} Z_k J_k \tag{7}$$

10　where i is the current density applied on the electrode. Substituting Eq. (1) into Eq. (7),

11　the following equation can be derived as:

12
$$\left(F/RT\right)\nabla U = -\frac{i + F\sum_{k=1}^{n} Z_k D_k \nabla C_k}{F\sum_{k=1}^{n} Z_k^2 D_k C_k} \tag{8}$$

13　and in a two-dimensional case, the current flow inside the concrete can be decomposed

14　into two components in the Cartesian coordinate (i.e., i_x and i_y), which can be

15　determined by $i_x=\partial U/\partial x$ and $i_y=\partial U/\partial y$ respectively. The electrostatic potential can be

16　solved by the Laplacian equation $\Delta U=0$.

17　　As for the current flow at the electrode surface, the boundary condition can be

18　determined as $i_b=\partial U/\partial n$, where n represents the normal direction of the boundary.

19　Moreover, the electrochemical reactions on the electrode surface should also be taken

1   into account to depict the ionic transport more accurately, which can be described as:

2
$$\text{for anode}\begin{cases} 4OH^- = 2H_2O + O_2 + 4e^- \\ 2H_2O = O_2 + 4H^+ + 4e^- \end{cases} \tag{9a}$$

3
$$\text{for cathode}\begin{cases} 2H_2O + O_2 + 4e^- = 4OH^- \\ 2H_2O + 2e^- = 2OH^- + H_2 \end{cases} \tag{9b}$$

4   Consequently, the quantity of consumption and generation of hydroxyl ions on the

5   electrode surface should follow the current conservation as

6
$$J_{OH^-}^b = \frac{i_b}{F} \tag{10}$$

7 **2.2 ASR cracking model**

8   At the initiation stage of the alkali silica reaction, alkalis like potassium and sodium

9   ions will diffuse into aggregates and react with silica to generate expansive gel.

10   Although the mechanism of alkali silica reaction is still controversial, we employ the

11   simplified formula proposed by Multon et al. [51] to depict the reaction rate as:

12
$$S_{Alk} = f \cdot \langle C_{Alk} - C_{thr} \rangle \tag{11}$$

13   where $\langle \rangle$ is defined as $\langle x \rangle = x$ if $x > 0$ and $\langle x \rangle = 0$ if $x \le 0$; S_{Alk} (mol/m^3/s)

14   represents the reaction rate of equivalent alkalis Na$_2$O$_{eq}$, which is two times of the

15   reactive term for sodium ions defined in Eq. (2) (since the reactive rate of equivalent

16   alkalis Na$_2$O$_{eq}$ equals two times of reactive rate of sodium S_{Na^+}); f (s^{-1}) represent the

17   fitting parameter for reaction rate which is taken as -6.5×10^{-7} s^{-1} [51]; C_{Alk} (mol/m^3) is

18   the concentration of the equivalent alkalis; C_{thr} (mol/m^3) is the threshold concentration

19   of alkali ions for the initiation of ASR , which is taken as 325 mol/m^3 at 23°C according

20   to literature [54].

21   The chemical reactions of ASR can be written in the net reaction from as Eq. (12).

1   Consequently, the total amount of expansive gel generated in each aggregate particle

2   (defined as domain Ω) equals to the total consumption of equivalent alkalis Na_2O_{eq}, and

3   can be determined by Eq. (13).

4
$$SiO_2 + 2OH^- \rightleftharpoons H_2SiO_4^{2-} \tag{12}$$

5
$$I_{gel} = \iint_{\Omega} \int_0^t S_{Alk} \, dt \, ds \tag{13}$$

6   where I_{gel} is the molar amount of expansive gel generated in one single aggregate

7   particle. Therefore, the free volumetric strain for each aggregate can be expressed as

8
$$\varepsilon_v = \frac{I_{gel} V_{gel}}{V_a} \tag{14}$$

9   where ε_v is the free volumetric strain without constrains; V_{gel} is the volume of ASR gel

10   per mole, which is taken as 18.2×10^{-6} m^3/mol; V_a is the volume of each particle.

11   The obtained volumetric strain is subsequently applied on alkali reactive

12   aggregates, and the corresponding cracking process of concrete composite is modelled

13   by cohesive element method. The basic principle of cohesive element methods is to set

14   cohesive elements one the interface of solid elements. When the failure criterion is

15   satisfied, the cohesive elements will be gradually damaged and eventually eliminated

16   to represent crack initiation and propagation. When modelling the cracking process, the

17   solid elements are first meshed to include three components of the concrete: cement

18   paste, coarse aggregates and rebar. Cohesive elements are then set on the interface

19   between cement paste and coarse aggregates to represent ITZ phase, and the weak

20   mechanical property of ITZ can also be characterized. Besides, cohesive elements are

21   also set inside the solid elements of cement phase to represent cracking of cement

1   matrix. Because the crack opening process is controlled by the failing behavior of

2   cohesive elements, its constitutive law should be firstly introduced and can be given as:

3
$$\begin{Bmatrix} t_n \\ t_s \end{Bmatrix} = \begin{bmatrix} k_n & 0 \\ 0 & k_s \end{bmatrix} \begin{Bmatrix} \delta_n \\ \delta_s \end{Bmatrix} \tag{15}$$

4   where t_n and t_s are tractions in normal and shear directions; k_n and k_s are element

5   stiffnesses in normal and shear directions; δ_n and δ_s are relative displacements in normal

6   and shear directions. For quasi-brittle material like concrete [55], cracks will initiate

7   when satisfying the quadratic nominal stress criterion as follows, and before that,

8   cohesive elements will behave as linear elastic.

9
$$\left\{ \frac{\langle t_n \rangle}{t_n^0} \right\}^2 + \left\{ \frac{t_s}{t_s^0} \right\}^2 = 1 \tag{16}$$

10   where t_n^0 is the maximum nominal stress for tensile cracking, and t_s^0 is the maximum

11   nominal stress for shear cracking. To describe the damage behavior under combined

12   action of tension and shear, the effective relative displacement δ_m is defined as

13
$$\delta_m = \sqrt{\langle \delta_n \rangle^2 + \delta_s^2} \tag{17}$$

14   and the bilinear softening law proposed by Bažant et al. [56] is adopted here, as shown

15   in Fig.2. δ_m^f is the effective relative displacement at complete failure of cohesive

16   elements, and δ_m^1 can be determined by the following condition: $G_{f2} = 1.5 G_{f1}$, where

17   G_{f1} and G_{f2} are fracture energies of the corresponding areas. The stiffness degradation
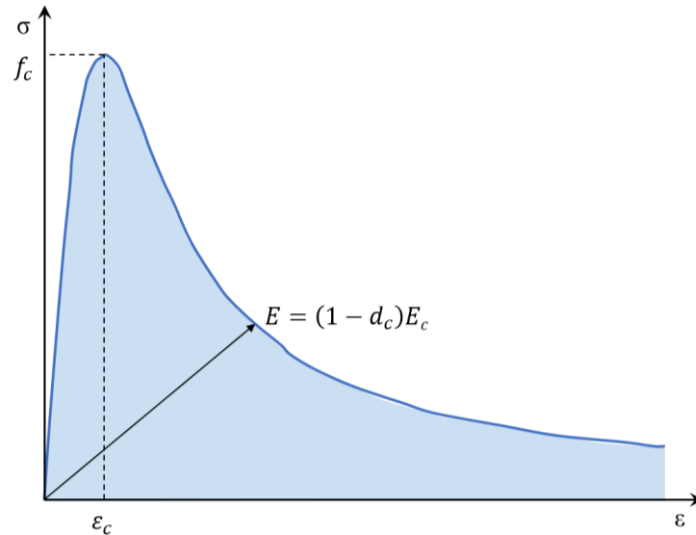
18   can be expressed by the tensile damage factor d_t as

19
$$\begin{cases} k_n = k_{n0}(1 - d_t) \\ k_s = k_{s0}(1 - d_t) \end{cases} \tag{18}$$

20   where k_{n0} and k_{s0} are initial element stiffness in normal and shear directions.
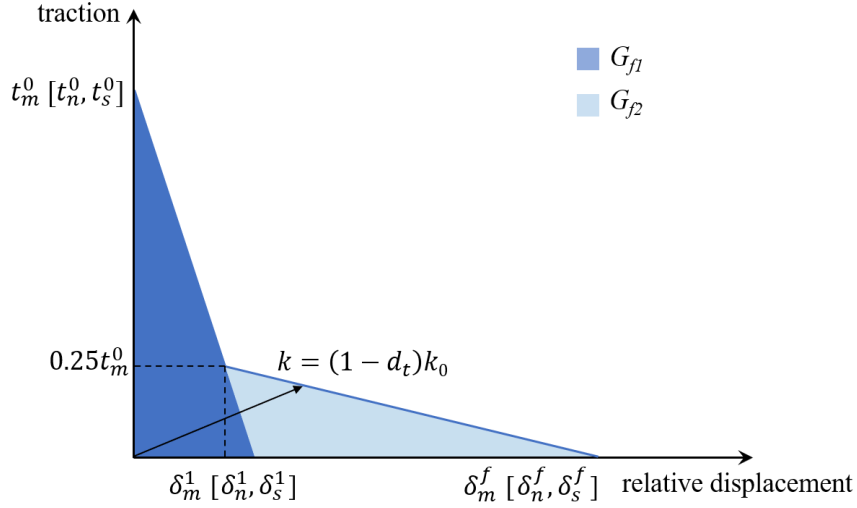
Fig.2 Schematic diagram of the bilinear softening law for cohesive elements.

Although the failure mode is generally tensile cracking for brittle materials like concrete, compressive plasticity still exists in real cases. However, it can be observed from Eq. (16) that, for cohesive elements, only the tensile and shear cracking is considered while the compressive mechanical property is assumed as linear elastic. Consequently, the concrete compressive plasticity should be reflected through the solid elements in this study, and the constitutive law adopted for the solid elements are calculated according to the Chinese code for design of concrete structures (GB 50010-2010), as shown in Fig.3. f_c represents the compressive strength of cement; ε_c represents the peak strain of cement; E_c represents the elastic modulus of cement paste; d_c represents the compressive damage factor. The element types and correspondingly adopted constitutive laws are concluded in Table 1.

|	Mechanical behavior		
	Compression	Tension	Shear
Element types	Solid elements	Cohesive elements	
Constitutive laws			

4   **2.3 Crack repair model**

5   Although various metal cations are suitable for electrochemical deposition

6   treatment, magnesium ions have been widely adopted due to the relative low cost and

7   easy access. In this study, $MgSO_4$ solution is selected as the external anolyte for

8   electrochemical deposition treatment. Once the ionic concentration product of

9   magnesium and hydroxyl ions in concrete pore solution, $C_{Mg^{2+}} \cdot C_{OH^-}^2$, exceed the

10   solubility product of magnesium hydroxide deposition, the previously free magnesium

11   and hydroxyl ions in the concrete pore solution will react to from depositions in solid

12   phase, which can be depicted as:

1 $$Mg^{2+}+2OH^- \leftrightharpoons Mg(OH)_2 \tag{19}$$
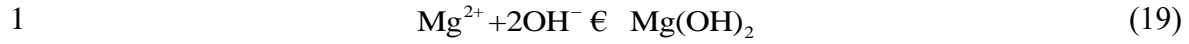
2 and the reaction rate can be subsequently calculated by

3 $$S_{Mg^{2+}} = k_r \cdot (C_{Mg^{2+}} \cdot C_{OH^-}^2 - k_{sp}) \tag{20a}$$

4 $$S_{OH^-} = 2k_r \cdot (C_{Mg^{2+}} \cdot C_{OH^-}^2 - k_{sp}) \tag{20b}$$

5 where $S_{Mg^{2+}}$ and S_{OH^-} represent the reaction rate for magnesium and hydroxyl ions

6 (i.e., reactive terms in Eq. (2)) respectively; k_r represents the deposition rate constant

7 which can be taken as 3.7×10^{-7} m^7/(mol$^2 \cdot$s) according to literature [57]; k_{sp} represent

8 the solubility product of magnesium hydroxide deposition which is taken as 0.45

9 mol^3/m^9 [57].

10 Before electrochemical deposition treatment, cracks can be regarded as completely

11 filled with pore solution, indicating that the porosity in crack region is 1. As the cracks

12 are gradually filled with deposition products, the porosity in crack region will gradually

13 decreases from 1 to a smaller value, which suggests that the porosity in crack region

14 can be used to characterize the crack closure rate as:

15 $$\psi_{crack} = 1 - \frac{M_{Mg(OH)_2}}{\rho_{Mg(OH)_2}} I_{Mg(OH)_2} \tag{21}$$

16 where ψ_{crack} is the porosity of crack area; $M_{Mg(OH)_2}$ and $\rho_{Mg(OH)_2}$ are the molar mass

17 and density of magnesium hydroxide, which have been taken as 0.058 kg/mol and 2450

18 kg/m^3 respectively; $I_{Mg(OH)_2}$ represents the molar amount of magnesium hydroxide

19 which can be calculated be the following integration.

20 $$I_{Mg(OH)_2} = \int_0^t S_{Mg^{2+}} dt \tag{22}$$

21 In addition to being formed in cracks, depositions will also be formed in pores to

22 improve the compactness of concrete, which will in turn retard the ionic transport

process. The time-dependent porosity can be expressed in a form similar to that of the crack region as:

$$\psi_t = \psi_0 - \frac{M_{Mg(OH)_2}}{\rho_{Mg(OH)_2}} I_{Mg(OH)_2} \tag{23}$$

where ψ_t represents the time-dependent porosity; ψ_0 represents the initial porosity before electrochemical deposition treatment. It should be noted that considering the porous nature of ITZ compared with the cement paste, the porosity of ITZ are larger than that of the cement paste [28, 58]. The relationships between porosities of ITZ, cement and concrete can be given by

$$\psi_{con,0} = \psi_{cp,0} V_{cp} + \psi_{ITZ,0} V_{ITZ} \tag{24}$$

where $\psi_{ITZ,0}$, $\psi_{cp,0}$ and $\psi_{con,0}$ denote the initial porosities of ITZ, cement paste and concrete respectively; V_{ITZ} and V_{cp} represent the volume fractions of ITZ and cement paste respectively. The initial porosity of ITZ can be determined by the empirical formula proposed in literature [59] as:

$$\psi_{ITZ,0} = \left(A_1 \cdot w / c + B_1 \right) \cdot A_2 \cdot V_{agg} + B_2 \tag{25}$$

where w/c represent the water cement ratio; A_1, A_2, B_1 and B_2 are dimensionless fitting parameters which have been taken as 55, 0.1, -27 and 40 respectively. Consequently, for cement paste and ITZ respectively, the change of diffusion coefficients caused by the porosity variances can be quantified by the Maxwell equation as

$$D_k^t = \frac{2\psi_t}{3 - \psi_t} D_k^0 \tag{26}$$

where D_k^t represents the time dependent diffusion coefficients for k-th ionic species; ψ_t represents the time-dependent porosity caused by deposition formation; D_k^t

represents the diffusion coefficients in water solution at 25 ℃.

3. Model establishment

3.1 Model guidelines

In this section, the previously introduced sub-models will be coupled to study the entire process from ASR-induced cracking to crack repair by electrochemical deposition method. Firstly, the ASR cracking process will be modelled with four initial phases: cement paste, ITZ, coarse aggregates and rebar, and the weak mechanical properties of ITZ are reflected by inserting cohesive elements between aggregates and cement paste. Considering ionic diffusion in alkali active aggregates, the consumption of alkalis and expansive volumetric strain can be calculated, and the crack distribution patterns during ASR attack period can be subsequently derived by ASR cracking model. Then, the ASR-induced cracks are included as a new phase in the crack repair model. Taking into account both ionic diffusion and migration, the crack repair status is characterized by the time varying porosity in crack area. Also, the consumption of magnesium and hydroxyl ions due to deposition reactions, and the time-dependent diffusion coefficients caused by deposition have been included. The modelling information is shown in Table 2. It should be noted that the aggregates are treated as impermeable in the crack repair model. This is because compared with the longer reaction time of ASR, the electrochemical deposition treatment commonly lasts for several weeks and applied with a relatively weak current density, so the ionic transport in aggregates are less obvious.

	ASR cracking model	Crack repair model
	Table 2 Modeling information for the entire process from ASR cracking to crack repair.	
Phases	Cement, aggregates, ITZ and rebar	Cement, ITZ, rebar and crack
Ionic transport	Diffusion	Diffusion and migration
Ionic consumption	Na^+ and OH^-	Mg^{2+} and OH^-
Governing equations	$\begin{cases} \dfrac{\partial C_{Na^+}}{\partial t} = D_{Na^+}\nabla^2 C_{Na^+} + \nabla[z_{Na^+}D_{Na^+}(\dfrac{F}{RT}\nabla\varphi)]C_{Na^+} + \dfrac{S_{Alk}}{2} \\[3mm] \dfrac{\partial C_{OH^-}}{\partial t} = D_{OH^-}\nabla^2 C_{OH^-} + \nabla[z_{OH^-}D_{OH^-}(\dfrac{F}{RT}\nabla\varphi)]C_{OH^-} + \dfrac{S_{Alk}}{2} \end{cases}$	$\begin{cases} \dfrac{\partial C_{Mg^{2+}}}{\partial t} = D_{Mg^{2+}}\nabla^2 C_{Mg^{2+}} + \nabla[z_{Mg^{2+}}D_{Mg^{2+}}(\dfrac{F}{RT}\nabla\varphi)]C_{Mg^{2+}} + S_{Mg^{2+}} \\[3mm] \dfrac{\partial C_{OH^-}}{\partial t} = D_{OH^-}\nabla^2 C_{OH^-} + \nabla[z_{OH^-}D_{OH^-}(\dfrac{F}{RT}\nabla\varphi)]C_{OH^-} + S_{OH^-} \\[3mm] (1+\xi)\cdot\dfrac{\partial C_{Cl^-}}{\partial t} = D_{Cl^-}\nabla^2 C_{Cl^-} + \nabla[z_{Cl^-}D_{Cl^-}(\dfrac{F}{RT}\nabla\varphi)]C_{Cl^-} \\[3mm] \dfrac{\partial C_k}{\partial t} = D_k\nabla^2 C_k + \nabla[z_k D_k(\dfrac{F}{RT}\nabla\varphi)]C_k \end{cases}$

Some basic assumptions made in the modelling process are concluded as follows:

1) Only the transport of sodium and hydroxyl ions are considered in the ASR-induced cracking model.

2) Expansive gel is uniformly distributed in the alkali reactive aggregates, and the expansion strain is the same in all directions.

3) Tensile and shear cracking is reflected through cohesive elements, and compressive plasticity is reflected by solid elements.

4) Aggregates are assumed as linear elastic without cracking due to the lack of relevant mechanical parameters.

5) Aggregates are regarded as permeable during ASR attack due to the longer span of reaction time (several years), while aggregates are considered as impermeable during the electrochemical deposition treatment due to shorter duration (couple of weeks).

6) Cracks can be regarded as completely closed when the porosity of crack area, ψ_{crack}, is below 0.55, which is consistent with the porosity of magnesium hydroxide depositions in literature [57].

3.2 Model setup

As for the geometrical representation, the model presented in this study is built in mesoscopic level with a dimension of 50 mm × 50 mm. The coarse aggregates are generated with a total volume fraction (V_{ca}) of 0.5 according to the Fuller grading curve, and the shape is adopted as random polygon to best comply with the aggregate shape in real cases. Then, the alkali reactive aggregates are randomly selected from the total amount of aggregates to reach the volume fraction of alkali reactive aggregates to total aggregates (V_{active}). Here, alkali reactive aggregates accounting for 30% of the total aggregate volume is illustrated as an example (i.e., V_{active} =30%), and the influence of alkali reactive aggregates volume fraction will be discussed in the next section.

As for the alkali silica reactions and subsequent cracking process, the transport of alkali ions into aggregates should be firstly explained. Here, the initial porosity of concrete, $\psi_{con,0}$, is taken as 0.2, and the initial porosities of ITZ and cement paste can be calculated as 0.33 and 0.40 according to Eq. (24) and Eq. (25). Because of the extremely low permeability of aggregates, the ionic diffusion coefficients in aggregates are set as 10^{-3} lower than these in cement paste [30, 51], as shown in Table 3. Moreover, the initial concentrations of alkali and hydroxyl ions in cement are also listed in Table 3. It should be noted that the initial ionic concentrations in aggregates are set as zero. Afterwards, the ASR-induced expansive strain can be determined by Eq. (14), and then applied on each alkali reactive aggregate to calculate the crack distribution patterns during ASR attack. Although concrete mechanical properties may vary under different scales [60], in the case of mesoscopic modelling in this study, the mechanical properties

1 used in the cracking model are listed in Table 4. Fig.4(a) illustrates the crack distribution

2 pattern after 500 days, where the red aggregates are alkali reactive aggregates taking up

3 30% of the total aggregate volume fraction. It can be observed that the ASR-induced

4 cracks generally initiate from the alkali reactive aggregates and connect with each other

5 to from cracks net.

6 **Table 3** Diffusion coefficients and initial ionic concentrations in concrete pore solution
7 for ASR cracking model (25°C) [61].

Ionic species	Initial concentrations in cement [mol/m^3]	Diffusion coefficients [m^2/s]			
		Water solution	Cement paste	ITZ	Aggregates
Na$^+$	500	1.33×10^{-9}	2.64×10^{-10}	3.13×10^{-10}	2.64×10^{-13}
OH$^-$	500	5.27×10^{-9}	1.04×10^{-9}	1.24×10^{-9}	1.04×10^{-12}

8 **Table 4** Mechanical properties adopted for solid and cohesive elements [62, 63].

	Solid elements			Cohesive elements	
	Cement paste	Coarse aggregates	rebar	Cement paste	ITZ
E [GPa]	30.2	70.3	210	-	-
v [-]	0.2	0.2	0.2	-	-
f_c [MPa]	40.4	-	-	-	-
Dilation angle (°)	38	-	-	-	-
Stress ratio (f_{b0}/f_{c0})	1.16	-	-	-	-
Eccentricity	0.1	-	-	-	-
k_{n0} and k_{s0} [MPa/mm]	-	-	-	10^6	10^6
t_n^0 and t_s^0 [MPa]	-	-	-	4.4	1.6
δ_m^f [mm]	-	-	-	0.071	0.098
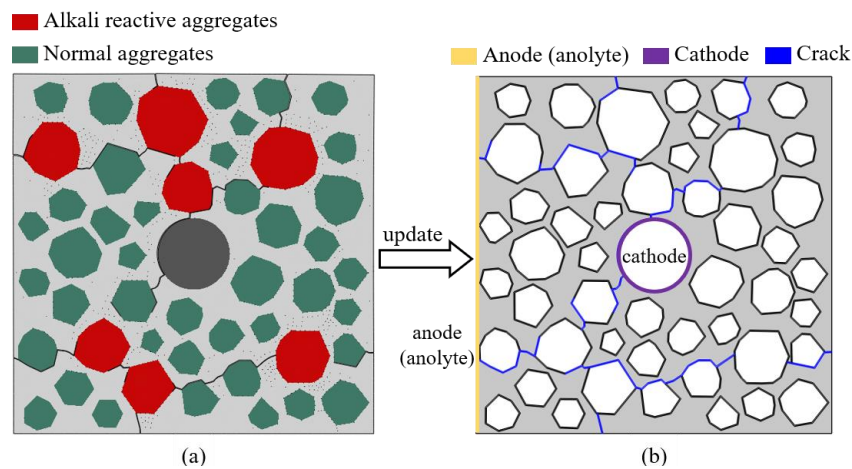
9 (a) (b)
10 **Fig.4** The geometry updating process from (a) crack distribution pattern caused by ASR
11 attack to (b) geometry for crack repair model.

1   Then, the calculated cracks from cacking model are included as a new phase in the

2   crack repair model. It should be noted that, in order to precisely reflect the influence of

3   crack tortuosity, the crack propagation directions have been carefully captured in the

4   crack repair model, and the updated geometry is shown in Fig.4(b). Because the time

5   span of electrochemical deposition treatment is relative shorter compared with the alkali

6   silica reaction which usually takes years, aggregates are assumed as impermeable in

7   crack repair model. The diffusion coefficients, anolyte concentration and initial ionic

8   concentrations is given by Table 5. During the electrochemical deposition treatment,

9   the magnesium hydroxide depositions continue to from in both cracks and concrete

10   pores, which will result in a time-dependent diffusion coefficients of various ions

11   involved in this process. Therefore, only the diffusion coefficients in water solution are

12   listed here. When modelling the ionic migration in cracked concrete, one has to consider

13   the influence of crack width on diffusion coefficients due to the current enrichment at

14   crack tips. However, the minimum crack width in this study is larger than 80 μm, which

15   has been reported to have negligible effects on diffusion coefficients [64].

16   **Table 5** Diffusion coefficients, initial and boundary concentrations for crack repair model
17   (25°C) [57, 61, 65].

Ionic species	Initial concentrations in cement	Boundary concentrations in anolyte	Diffusion coefficients in water solution
K^+	300 mol/m^3	50 mol/m^3	1.96×10^{-9} m^2/s
Na^+	300 mol/m^3	5 mol/m^3	1.33×10^{-9} m^2/s
Mg^{2+}	-	100 mol/m^3	0.75×10^{-9} m^2/s
Cl^-	300 mol/m^3	5 mol/m^3	2.03×10^{-9} m^2/s
OH^-	300 mol/m^3	50 mol/m^3	5.27×10^{-9} m^2/s
SO_4^{2-}	-	100 mol/m^3	0.38×10^{-9} m^2/s

4. Model validation

In this section, the validity of the presented numerical model is verified from three key aspects, i.e., expansion rate, crack closure rate and chloride removal efficiency. Considering that the volume expansion rate of alkali reactive aggregates is difficult to be measured by experimental procedure, and most of the experimental results on expansion rate are conducted at macro scale rather than meso scale, the empirical formula [66] fitted from Larive's experiments [67], which was also adopted in the macroscopic modelling by Kawabata et al. [68], and mesoscopic modelling by Pan et al. [69], is selected herein for validating the expansion rate of alkali reactive aggregates. As for the cases of crack closure rate and chloride removal efficiency, the data from electrochemical deposition experiments conducted by Chu et al. [45] and Ryu et al. [43] are used to verify the crack closure rate and chloride removal efficiency respectively.

4.1 ASR expansion rate

The volumetric expansion of alkali reactive aggregates calculated by ASR cracking model is compared with the empirical formula proposed by Ulm et al. [66], as shown in Fig5. Note that only the volumetric expansions of three representative alkali silica reactive aggregates are shown for better visual effect, and the expansions of other aggregates are between the upper and lower limits. In addition, because the maximum volume expansion depends on the alkali contents and alkali activity of aggregates, the expansion is normalized according to the maximum expansion rate calculated by the empirical formula. It can be observed that the aggregate volume expansions calculated by our model are in good consistence with the empirical formula. With the ingress of

1   alkalis into aggregates, the expansive gel is firstly generated in the outer layer while the

2   alkalis concentration in the inner part is still below the threshold value for ASR

3   initiation. Then, with more alkali diffuse into aggregates, the expansive gel will also be

4   generated inside the aggregate, causing a rapid increase in expansion rate. In the later

5   stage, the alkalis concentration gradually decreases below the threshold value because

6   of the continuous consumption, and the expansion rate will gradually slow down.
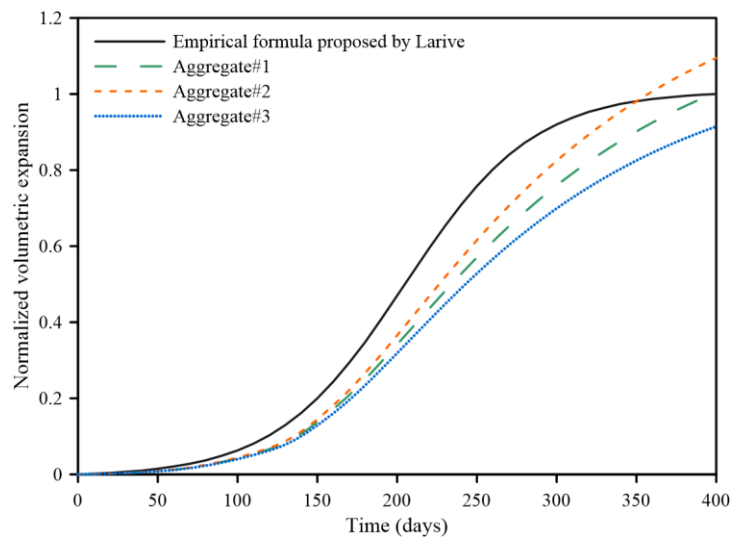
Fig.5 Comparison of numerical and empirical results for aggregates volumetric expansion.

4.2 Crack closure rate

The crack closure rate is defined as the area ratio between the completely closed

area to the total area of cracks. The experimental results of Chu et al. [45] is adopted to

further verify the crack closure rate calculated by the crack repair model. In the

experiment, the specimen was immersed in the 250 mol/m^3 MgSO$_4$ solution for 20 days

with a direct current density of 2.0 A/m^2. The comparison between experimental and

numerical results is shown in Fig.6 where the red region of the crack represents the

completely repaired part (i.e., the porosity has been lower than 0.55), and the blue

region represents the porosity is still above 0.55. The load-induced crack is calculated

1 by the cracking model by adding bending moment on both sides, and the crack widths

2 on the specimen surface is 0.3 mm which is in accordance with that measured in the

3 experiment. It can be seen that our numerical results basically agree with the

4 experimental results. In addition, it can be found that the crack repair rate increased the

5 fastest in the first five days, and gradually became flat in the later stage of the treatment.

6 This is because the deposition can compact concrete pore structures and close

7 previously exposed cracks, which can block the subsequent supply of magnesium ions

8 and lead to a decreased deposition rate.
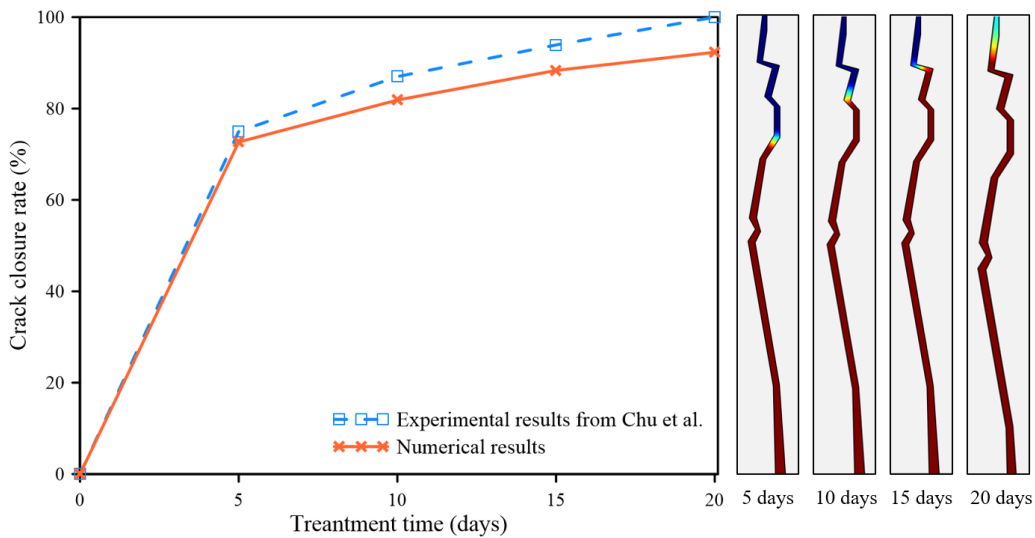
9

10   **Fig.6** Comparison of numerical and empirical results for crack closure rate.

11 **4.3 Chloride removal efficiency**

12   In addition to crack closure, the chloride can also be removed from concrete under

13 the effect of externally applied electric field. Therefore, chloride removal efficiency is

14 another index to evaluate the effect of electrochemical deposition treatment. Fig.7

15 illustrates the comparison of the normalized chloride concentration ($C_{Cl^-}/C_{Cl^-,0}$) around

16 the steel reinforcement surface between the experimental data of Ryu et al. [43] and our

17 numerical results. It can be observed that the final chloride removal efficiency shows

26

great agreement with the experimental data after the 8-week electrochemical deposition treatment. Nearly 80% of the chloride have been removed from the rebar surface, which indicates that the corrosion risk of embedded rebars can be greatly reduced. Nevertheless, relatively large difference can be observed in the middle of treatment. This can be explained by the fact that transverse cracks may appear in the experiment specimens, which can facilitate the chloride removal process to some extent. However, with the closure of cracks, the promoting effect of cracks on chloride removal will be no longer obvious, and the final numerically predictive result is close to the experimental data.
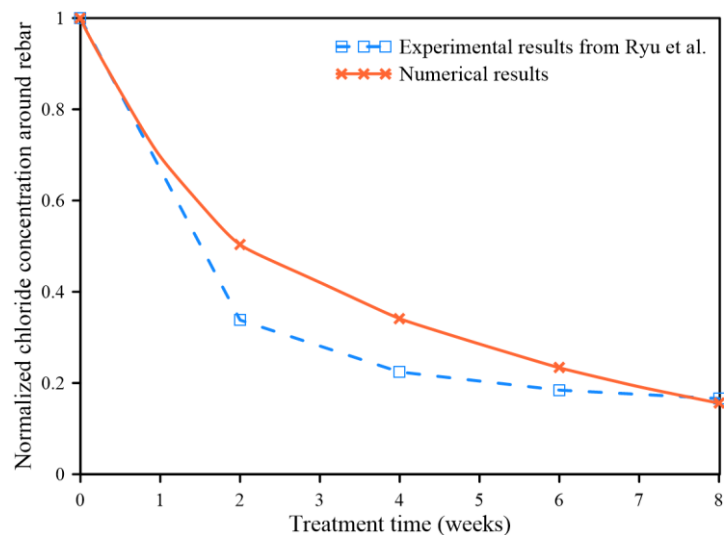
Fig.7 Comparison of numerical and empirical results for chloride removal efficiency.

5. Discussion

5.1 Overview

In order to deeply reveal the interconnections among various potential influencing factors, a parametric analysis is conducted in this section. At first, some general results will be discussed to reveal features of ASR-induced cracking and electrochemical deposition repair on ASR-induced cracks as well. The initial concentrations and

27

1   diffusion coefficients are adopted as the same with those mentioned in Section 3.2. The

2   current density applied on the cathode surface (embedded rebar) is initially set as 2.0

3   A/m^2; the anolyte concentration is selected as 500 mol/m^3, and the percentage of alkali

4   active aggregate in total aggregate volume is 30%. Detailed analysis on the influence

5   of the abovementioned three factors will be discussed in the following sections.

6   The ionic distribution profile of sodium ion during ASR and the corresponding

7   cracking process is shown in Fig.8. It can be observed that the cracking process has an

8   obvious delayed phenomenon to the alkali silica reactions. It is until the middle of ASR

9   reaction (around 350 days after the initiation of ASR) that macro cracks start to appear.

10   This is because the internal strain caused by the expansive gel has not reached the

11   concrete cracking strain, and the concrete will still remain sound. However, once the

12   cracks initiate, it will develop rapidly after initiation (as seen from 350 days to 450

13   days), which may cause failure of structural bearing capacity in a short period of time.

14   Therefore, it is significant to predict the failure process and rehabilitate the structures

15   with potential ASR risks in time. In addition, it can be also observed that due to the

16   consumption of sodium ions, the diffusion in alkali reactive aggregates is slower than

17   that in normal aggregates. The ASR-induced cracks generally initiate from alkali

18   reactive aggregates and develop along ITZ. It indicates that the weak mechanical

19   properties make ITZ as a weak link for crack propagation.
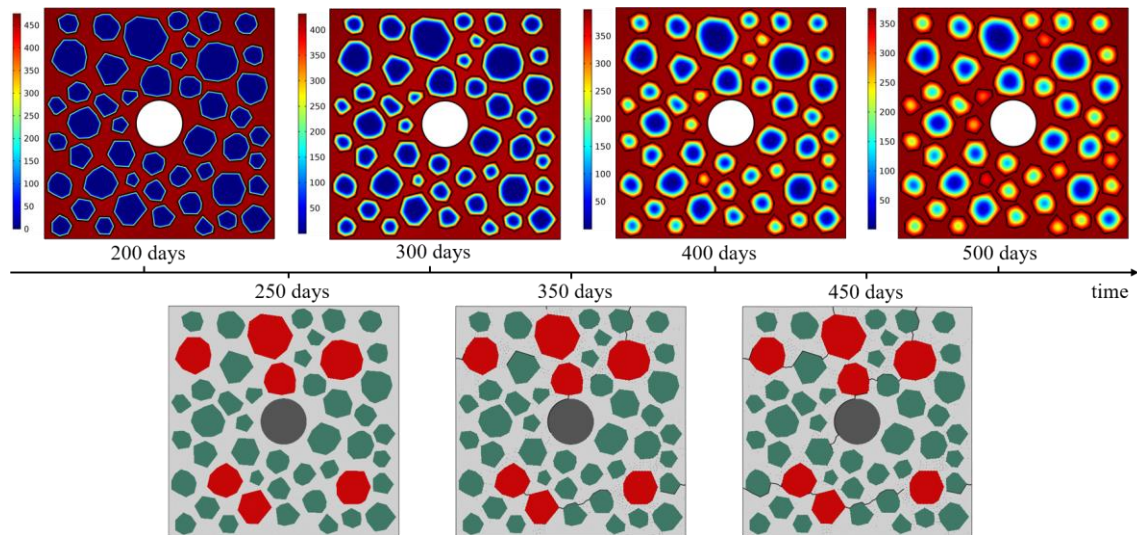
Fig.8 The alkali ion distribution profile and ASR-induced cracking process over time.

The crack closure rate with the left side serving as anode (i.e., magnesium ions migrate from left to right) is shown in Fig.9. It can be observed that when the anolyte is only arranged on the left side, the crack repair rate is not ideal, and only less than 20% of the cracks have been repaired. In fact, it is the cracks near to the anode that can be effectively repaired, while cracks distributed in the inner part of the concrete still remain opened. This is because, on the one hand, depositions generated on the concrete surface will mitigate the transport of magnesium ions into deeper cracks. On the other hand, cracks induced by ASR possess a more random distribution pattern compared with these induced by load, so cracks near to the other three surfaces cannot get efficient repair. Therefore, for electrochemical deposition treatment on ASR-induced cracks, the anode position should consider the crack distribution patterns. For structural components like column whose surfaces are all exposed, the anode should arrange on the all four surfaces to get the best repair effect. The selection of anode position will be discussed in the following section.
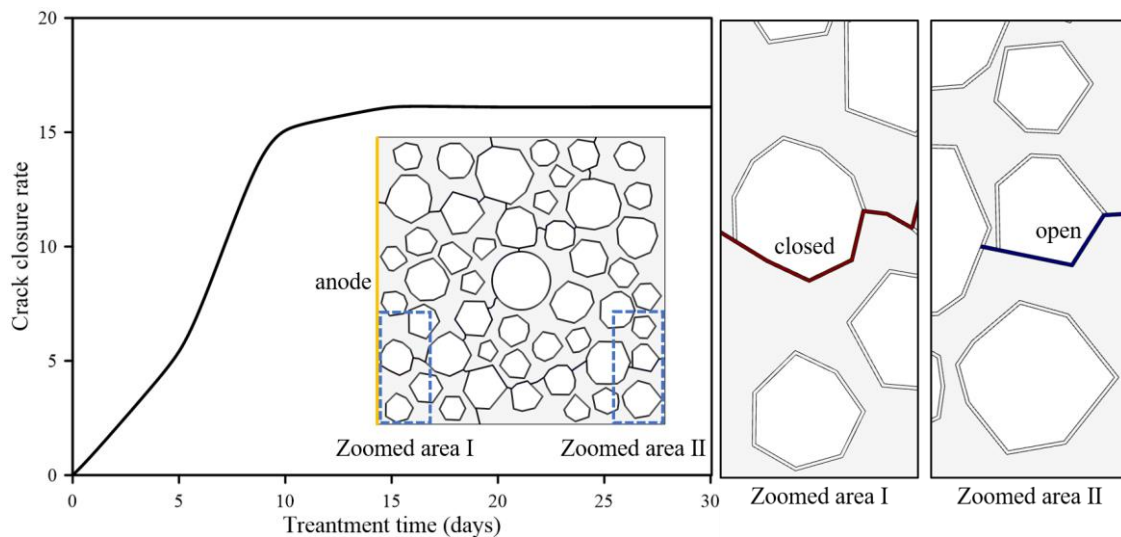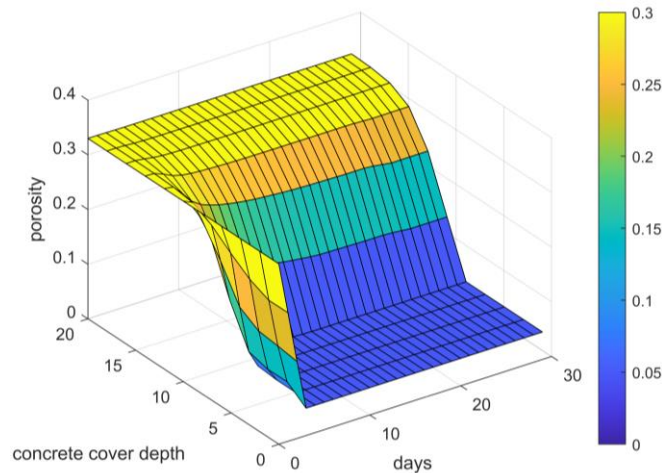
Fig.9 The crack closure rate over time when anode is set on the left.

The time-dependent cement porosity in different cover depths during the electrochemical deposition treatment is shown in Fig.10. The porosity in cement paste is initially calculated as 0.33, and the subsequent reduction caused by magnesium hydroxide deposition generation can be determined by Eq. (26). It can be seen that the porosity in the outer layer of concrete cover can be significantly decreased from the initial value 0.33 to nearly 0 in the first five days during the treatment. It suggests that the concrete surface which is immersed in the anolyte can be effectively coated by electrochemical deposition method, and the refined pore structures can prevent the ingress of deleterious agents like chloride and sulfate ions. Also, the subsequent migration of magnesium ion is also blocked by the reduced porosity, so the crack closure rate increases rapidly at the initial stage of treatment but then tends to be stable. However, for concrete cover depth larger than 10 mm, the porosity basically remains constant from the 10th day of the treatment, and for concrete cover depth larger than 15 mm, the porosity will not change, suggesting that there is little deposition generated at this depth. Consequently, it can be concluded that in order to completely close deeper

1   cracks, it is always recommended to set more exposed surface as anodes.

3   **Fig.10** Time-dependent cement porosity at different concrete cover depths during the
4   electrochemical deposition treatment.

5   **5.2 Anode electrode position**

6   In order to investigate the optimal anode arrangement, the crack closure rates under

7   four cases with different anode positions arrangement are compared in Fig.11. Anode

8   is set on the left surface for Case 1; anode is set on both left and right surfaces for Case

9   2; anode is set on both the up and down surfaces for Case 3, and anode is set on all

10   surfaces for Case 4. It can be seen that the anode arrangement in Case 1 has the lowest

11   crack closure rate, and this is because the cracks distributed on the opposite side of the

12   anode are difficult to get closed. Besides, Case 2 and Case 3 show similar results in

13   crack closure rates, and the final repair rate is only a little higher than that of the Case

14   1. However, when arranging anode on all exposed surfaces, the crack closure rate shows

15   significant improvement compared with the other three cases. This is because, for

16   cracks caused by ASR, it will be randomly distributed near four surfaces, so it is difficult

17   to repair the cracks penetrating other surfaces by arranging only one surface as the

18   anode. Therefore, for electrochemical deposition treatment on ASR-induced cracks,

1   setting all exposed surfaces as anode can improve the crack repair efficiency and

2   maximum repair rate.
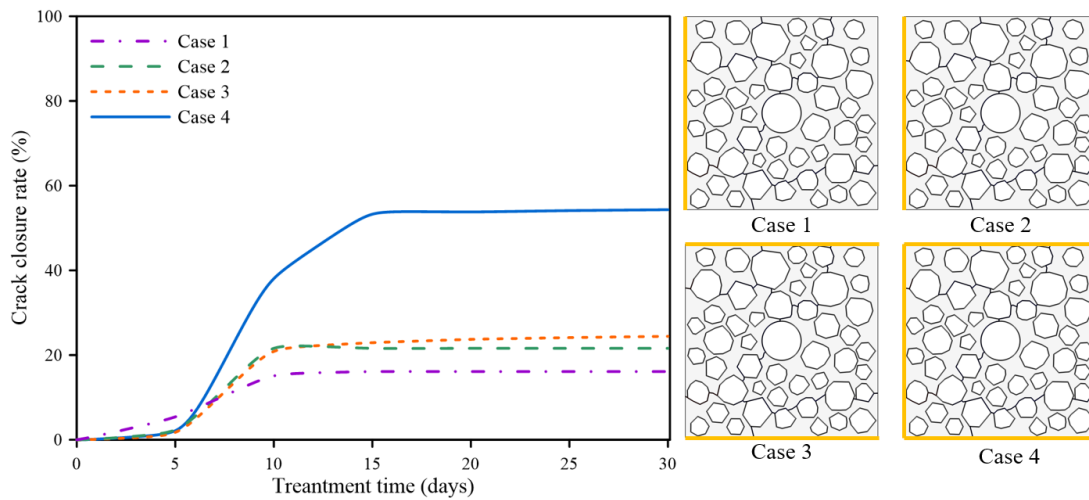

3

4   **Fig.11** Crack closure rates with various anode arrangements.

5   **5.3 Volume fraction of alkali-active aggregates**

6   *5.3.1 Impact on crack distribution patterns*

7   When the volume fraction of alkali active aggregates in the total aggregates, V_{active},

8   is 10%, 30%, 50%, 70% and 90%, the corresponding crack distribution patterns are

9   shown in Fig.12, where the red aggregates represent the alkali reactive particles suffered

10   from ASR, and the green aggregates represent the normal aggregates. It can be seen that

11   the cracks basically initiate from the ASR attacked aggregates and develop along the

12   weak link formed by ITZ. Besides, crack will not initiate at the beginning of alkali silica

13   reaction, while it is delayed until the middle period of alkali silica reaction, and cracks

14   will propagate rapidly in the remaining time. In addition, it can be observed that with

15   the increase of the volume fraction of alkali reactive aggregates, the cracks will form a

16   more connected crack network, which is more deleterious to structural carrying capacity.

17   On the other hand, it is found that cracks caused by the larger volume fraction of alkali

1 reactive aggregates have a more random distributed pattern, indicating that the anode

2 position is recommended to set on all exposed surfaces to get a better healing effect.
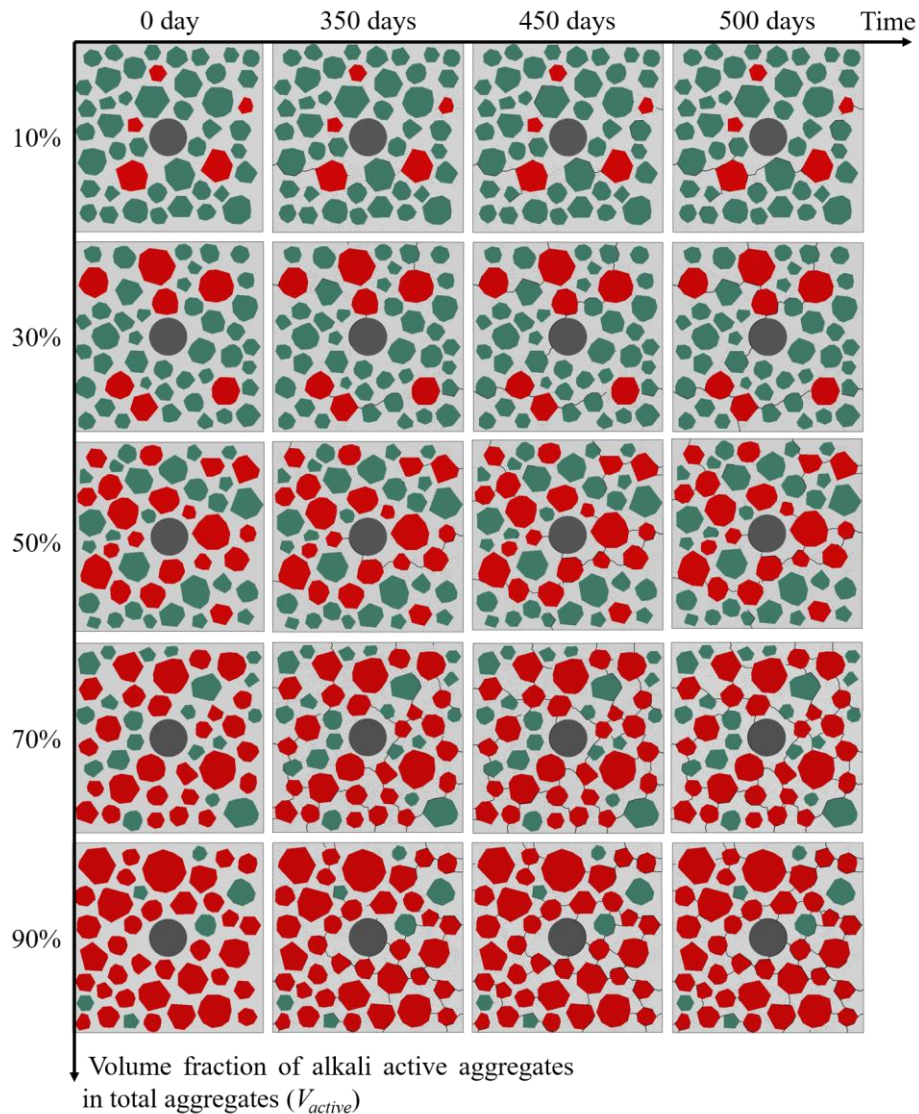
3

4 **Fig.12** Crack distribution patterns under various volume fractions of alkali reactive
5 aggregates.

6 *5.3.2 Impact on crack length and volume*

7 The total length of ASR-induced cracks is shown in Fig.13 as a function of time.

8 Generally, it can be found that with the increase of V_{active}, the crack initiation time will

9 be slightly earlier but still in the middle period of the alkali silica reaction. Moreover,

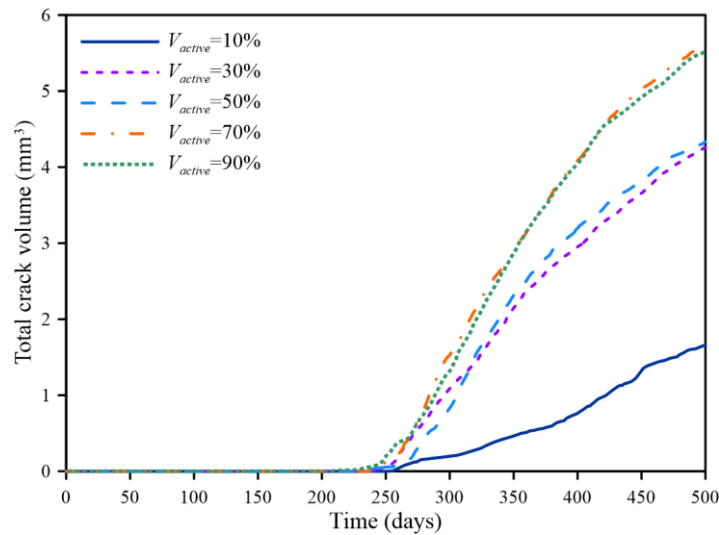10 more alkali reactive aggregates will lead to a longer crack length, suggesting that the

33

ultimate concrete damage degree is more serious. However, the increase of crack length

is less obvious when V_{active} has exceeded 70%. Besides, the maximum increase is found

between 10% and 30%, and the total crack length with 30% volume fraction is twice of

that with 10%.

The crack volumes with alkali reactive aggregates taking up 10%, 30%, 50% 70%

and 90% in total aggregates are shown in Fig.14. Although most features of crack

volumes are similar to those of crack length, less variations of crack volumes can be

observed between 30% V_{active} and 50% V_{active}, which is different to the variations of

crack lengths between 30% V_{active} and 50% V_{active}. Considering the similar crack volume

and longer crack length of 50% V_{active} compared to those of 30% V_{active}, it can be inferred

that the crack width of 50% alkali silica reactive aggregates are narrower than that of

30%. In addition, it can be found, from both the crack length and volume, that when the

volume fraction of alkali reactive aggregates in total aggregates has exceeded 10%, the

ASR-induced damage will deteriorate rapidly. However, when the volume fraction is

10%, the damage will involve in relatively mild manner. Consequently, it can be

concluded that silica active aggregates volume fraction larger than 10% can lead to

more serious and rapid damage of concrete structures.
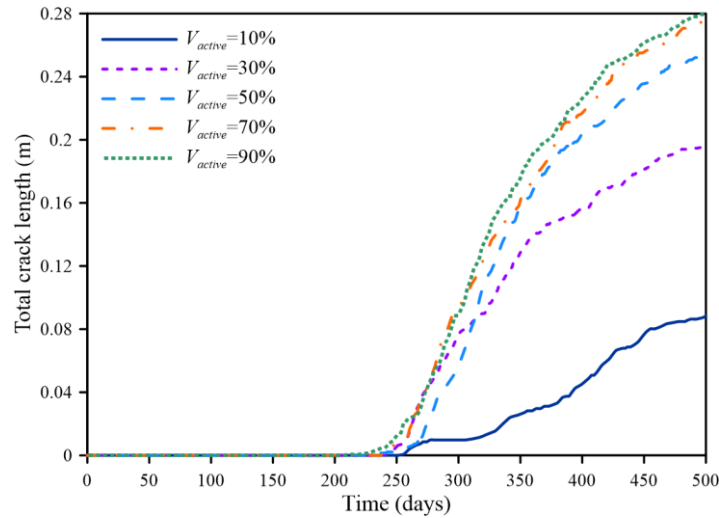
Fig.13 Crack lengths for various volume fractions of alkali reactive aggregates.
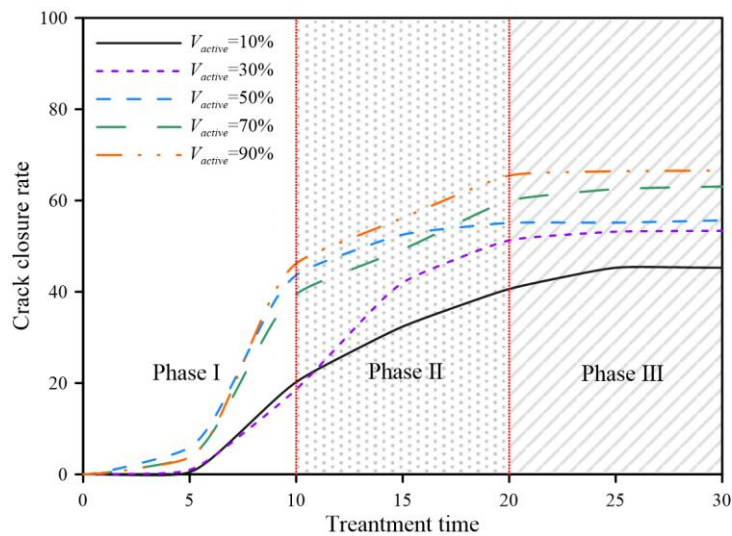

Fig.14 Crack areas for various volume fractions of alkali reactive aggregates.

5.3.3 Impact on crack closure rates

When the four sides are all set as anode, the crack repair rates for various volume fractions of alkali reactive aggregates are shown in Fig.15. Generally, the crack repair rate over time can be divided into three phases. Phase I is featured by a rapid increase in crack closure rate in the first 10 days during the treatment. This is because for ASR attacked concrete, the hydroxyl ions are still abundant in concrete pore solution, and will react with migrated magnesium ions to form depositions and close cracks. In Phase II, however, the growth rate of crack repair rate decreases gradually, which can be

explained by the following aspects. Firstly, the hydroxyl ions have been gradually

depleted, which can reduce the deposition reaction rate. secondly, the magnesium

hydroxide deposition can also coat the concrete surface and block the subsequent

transport of magnesium ions. As for Phase III, crack closure rates remain stable and

further increase cannot be observed. This is because with the gradual refinement of

pores structures, the magnesium ions are harder to migrate into internal cracks. Besides,

it can be found that with the increase of the volume fraction of alkali reactive aggregates,

the closure rate after 30-day treatment is higher. This is because larger aggregates

volume fraction suffered from ASR attack can produce a more connected cracks

network, which can facilitate the ionic transport to some extent.

Fig.15 Crack closure rates under various volume fractions of alkali reactive aggregates.

5.4 Current frequency

In addition to the direct current density, periodic current density has also been

commonly adopted for electrochemical deposition treatment and electrochemical

chloride extraction [45, 70]. Here, when all four surfaces are set as anode, the crack

closure rates under pulse current with three different periodic characteristics are

36

1   compared with the closure rate under direct current, as shown in Fig.16. In Case 1, the

2   pulse current on-time and off-time are both 1 day with a 2 A/m^2 maximum amplitude;

3   In Case 2, the pulse current on-time is 1 day with a 2-day interval; In Case 3, the pulse

4   current on-time is 2 days with a 1-day interval; and the direct current amplitude is also

5   2 A/m^2. It can be observed that in the middle of treatment, closure rate of pulse current

6   is generally lower than that of direct current. It is mainly caused by the time-off period,

7   which can mitigate the ionic migration process and delay the crack closure. In addition,

8   it can be seen from the figure that the pulse current with 1-day on and 2-day off can

9   reach the similar repair rate of direct current at the end of the treatment, and the pulse

10   current with 1-day on and 1-day off shows the best repair rate. This is because the time-

11   off period can prevent the premature coating of concrete surface, and hence prolongs

12   the time for magnesium ions entering the concrete.
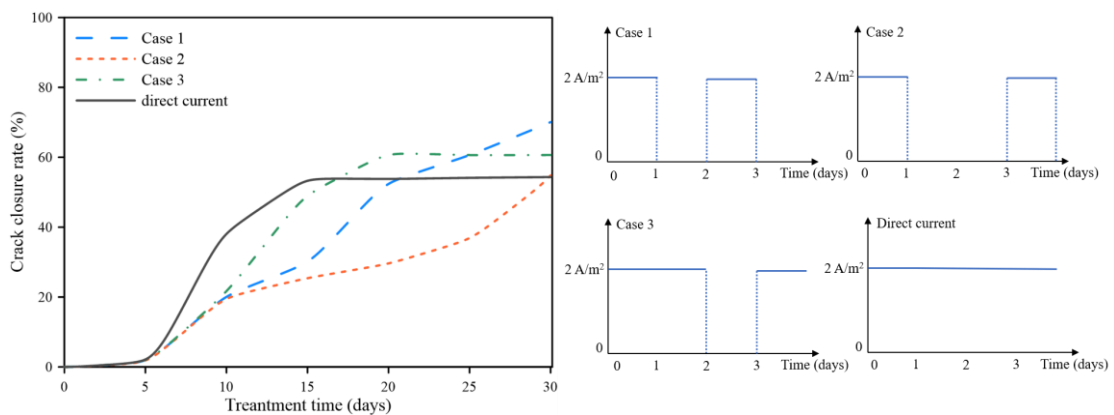
13
14   **Fig.16** Crack closure rates under various current density frequencies.

15   The magnesium ion concentrations at 5 mm depth of concrete cover under different

16   current frequencies are shown in Fig.17. It can be seen that pulse current can lead to

17   higher magnesium ion concentration compared with direct current, which is caused by

18   the fact that the off-time duration can ensure the transport of more magnesium ions into

1   concrete. This phenomenon also verifies our explanation on the better repair effect of

2   pulse current. Additionally, it can be found that the magnesium ion concentration under

3   direct current shows a decreased trend from the 10th day of the treatment, but

4   magnesium ion concentration under pulse current shows a stable trend with slight

5   fluctuations. The fluctuations are mainly caused by the current switch on and off, and

6   the more stable concentration indicates that the supply of magnesium ion concentration

7   can be better ensured.
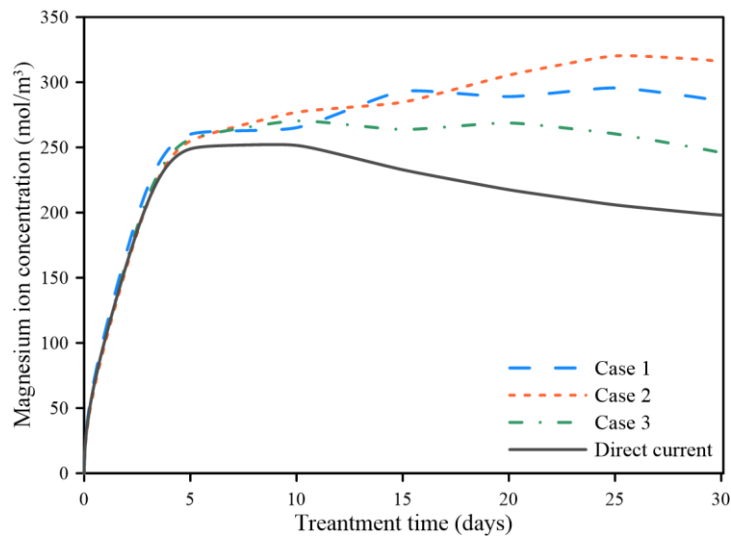
8

9   **Fig.16** Magnesium ion concentration under various current density frequencies.

10   **5.5 Current amplitude**

11   With all four surfaces setting as anode, the crack closure rates under various current

12   density amplitudes of 0.5 A/m^2, 1.0 A/m^2, 2.0 A/m^2 and 4.0 A/m^2 applying on the

13   embedded steel reinforcement are compared in Fig.18. It can be seen that the smaller

14   current density amplitude can result to a higher crack closure rate. This is also because

15   the larger current density amplitude will prematurely coat the concrete surface and

16   mitigate the subsequent magnesium transport. However, it does not suggest the smaller

17   current density amplitude should always be preferred in practical engineering. Although

1 the lower current density possesses better crack repair effect, the chlorine removal

2 efficiency of lower current density is inferior to that of larger current density, and may

3 need more treatment time to achieve the expected chloride extraction effect [71].

4 Besides, it should be noted that the excessively large current density amplitude is either

5 not recommended especially for RC structures subjected to ASR attack. This is because

6 the hydroxyl ions will be generated on the cathode (embedded rebar) surface because

7 of the electrochemical reactions, which will severe the alkali silica reaction.
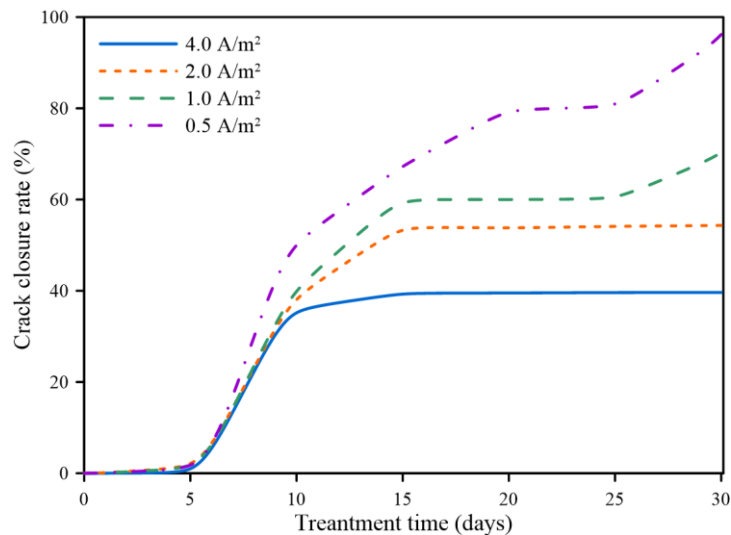

8
9 **Fig.18** Crack closure rates under various current amplitudes.

10 **5.6 Anolyte concentration**

11 In addition to the anode arrangement, anode solution concentration can also

12 influence the crack closure rates. Fig.19 illustrates the crack closure rates under four

13 different anode solution concentrations with all exposed surfaces set as anode. It can be

14 found that 500 mol/m^3 magnesium hydroxide solution possesses the lowest closure rate,

15 while the 200 mol/m^3 magnesium hydroxide solution can close approximate 70%

16 cracks. It indicates that the lower concentration can lead to higher crack closure rate,

17 which is consistent with experimental observation in literature [46]. This is because

1 higher anolyte concentrations can lead to an earlier deposition formation on the concrete

2 surface and hence block the transport process of magnesium ions into deeper concrete

3 where cracks distribute. For anolyte with lower concentration, however, magnesium

4 ions can transport into the deeper cracks without blocking during the treatment period.

5 Moreover, it can be seen that the improvement on crack closure rate is not obvious

6 between 200 mol/m^3 and 300 mol/m^3 anolytes. This can be explained by the fact that

7 the transport of magnesium has been controlled by the migration, and the diffusion

8 caused by concentration gradient is no longer dominant when the anolyte concentration

9 is excessively low.
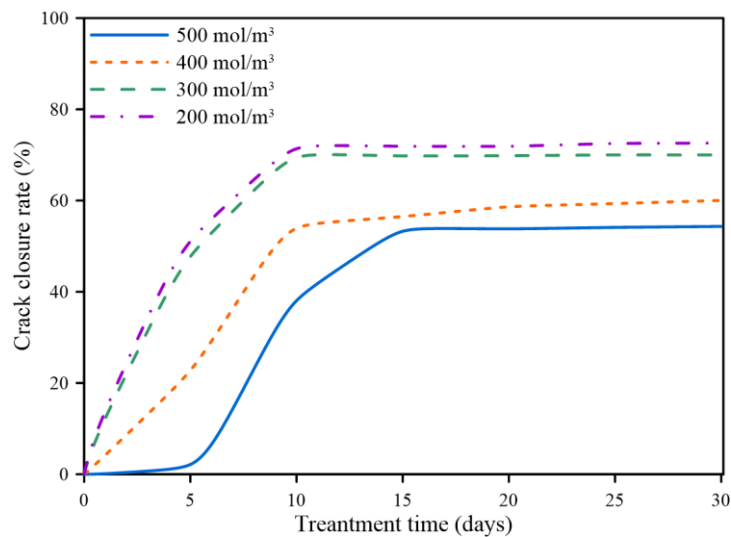
10

11 **Fig.19** Crack closure rates under various anode solution concentrations.

12 ## 6. Conclusions

13   In this study, the entire process from ASR-induced concrete cracking to crack repair

14 by electrochemical deposition repair method is numerically modelled for the first time.

15 Three internally coupled sub-models: multi-ionic transport model, ASR cracking model

16 and crack repair model have been proposed to reveal the underlying mechanisms from

17 a fundamental point of view. The ionic consumption during ASR and electrochemical

deposition treatment are quantitively considered and coupled into ionic transport model. In the cracking model, the weak mechanical property of ITZ is reflected by cohesive elements set between aggregates and cement paste. The compressive plasticity is reflected through solid elements, which is hoped to make up for the disadvantage that the cohesive elements cannot consider the compressive plasticity. In the crack repair model, the crack closure rate is characterized by the time-dependent porosity, and the variations of diffusion coefficients caused by deposition precipitation has also been taken into account. The proposed model is validated by experimental results, and a subsequent parametric analysis is carried out to provide guidance to the actual application of electrochemical deposition method. Some important findings obtained from our numerical model can be concluded as follows:

1) The electrochemical deposition method can effectively close the ASR-induced cracks and remove chloride ions to prevent corrosion of steel reinforcements. The concrete cover can be coated by deposition products, and pore structures can also get refined, which is helpful to resist the ingress of harmful agents.

2) There is a delayed phenomenon between alkali silica reaction and concrete cracking, and cracks will not initiate until the middle stage of the alkali silica reaction. The increase in the alkali reactive aggregates volume fraction can lead to larger crack area, longer crack length and more connected fracture network, and the most serious damage increase is between 10% and 30% alkali reactive aggregates volume fractions.

3) Both the anode solution concentration and anode electrode position influence

the crack repair rate. For electrochemical deposition treatment on ASR-induced cracks, setting all exposed surfaces as anode and immersing into lower concentration anolyte can lead to a better crack closure effect.

4) The crack closure rates are also influence by the current density amplitude and frequency. Lower current density can improve the crack repair rate while prolong the treatment duration to reach the expected chloride removal effect. Periodic current like pulse current can ensure the subsequent supply of magnesium ions into concrete and thus improving the final crack closure rate.

Admittedly, the presented numerical model still has some limitations and is hoped to be improved in the future work. Firstly, the influence of ambient temperature on the electrochemical reactions can be taken into account to better depict the reaction behaviors. Secondly, the two-dimensional model can be upgraded to a three-dimensional one. Finally, the mechanical properties and durability after electrochemical deposition treatment also need investigation in the future work.

Acknowledgements

References

[1] Zahedi A, Trottier C, Sanchez LFM, Noel M. Microscopic assessment of ASR-affected concrete under confinement conditions. Cement Concrete Res. 2021;145.

[2] Santos MB, de Brito J, Silva AS, Ahmed HH. Study of ASR in concrete with recycled aggregates: Influence of aggregate reactivity potential and cement type. Constr Build Mater. 2020;265.

[3] Kawabata Y, Dunant C, Yamada K, Scrivener K. Impact of temperature on expansive behavior of concrete with a highly reactive andesite due to the alkali-silica reaction. Cement Concrete Res. 2019;125.

[4] Rezakhani R, Alnaggar M, Cusatis G. Multiscale Homogenization Analysis of Alkali-Silica Reaction (ASR) Effect in Concrete. Engineering. 2019;5:1139-54.

[5] Gorga RV, Sanchez LFM, Martin-Perez B. FE approach to perform the condition assessment of a concrete overpass damaged by ASR after 50 years in service. Eng Struct. 2018;177:133-46.

[6] Rajabipour F, Giannini E, Dunant C, Ideker JH, Thomas MDA. Alkali-silica reaction: Current understanding of the reaction mechanisms and the knowledge gaps. Cement Concrete Res. 2015;76:130-46.

[7] Iskhakov T, Timothy JJ, Meschke G. Expansion and deterioration of concrete due to ASR: Micromechanical modeling and analysis. Cement Concrete Res. 2019;115:507-18.

[8] Wu HT, Pan JW, Wang JT. Nano-scale structure and mechanical properties of ASR products under saturated and dry conditions. Sci Rep-Uk. 2020;10.

[9] Collins CL, Ideker JH, Willis GS, Kurtis KE. Examination of the effects of LiOH, LiCl, and LiNO3 on alkali-silica reaction. Cement Concrete Res. 2004;34:1403-15.

[10] Diab SH, Soliman AM, Nokken MR. Changes in mechanical properties and durability indices of concrete undergoing ASR expansion. Constr Build Mater. 2020;251.

[11] Giaccio G, Zerbino R, Ponce JM, Batic OR. Mechanical behavior of concretes damaged by alkali-silica reaction. Cement Concrete Res. 2008;38:993-1004.

[12] Savija B, Pacheco J, Schlangen E. Lattice modeling of chloride diffusion in sound and cracked concrete. Cement Concrete Comp. 2013;42:30-40.

[13] Peng C, Wu Q, Shen J, Mo R, Xu J. Numerical study on the effect of transverse crack self-healing on the corrosion rate of steel bar in concrete. J Build Eng. 2021;41.

[14] Xu J, Peng C, Wan LJ, Wu Q, She W. Effect of Crack Self-Healing on Concrete Diffusivity: Mesoscale Dynamics Simulation Study. J Mater Civil Eng. 2020;32.

[15] Zhang YM, Zhuang XY. A softening-healing law for self-healing quasi-brittle materials: Analyzing with strong discontinuity embedded approach. Eng Fract Mech. 2018;192:290-306.

[16] Balzano B, Sweeney J, Thompson G, Tuinea-Bobe CL, Jefferson A. Enhanced concrete crack closure with hybrid shape memory polymer tendons. Eng Struct. 2021;226.

[17] Tissier Y, Bouteiller V, Marie-Victoire E, Joiret S, Chaussadent T, Tong YY. Electrochemical chloride extraction to repair combined carbonated and chloride contaminated reinforced concrete. Electrochim Acta. 2019;317:486-93.

[18] Otsuki N, Ryu JS. Use of electrodeposition for repair of concrete with shrinkage cracks. J Mater Civil Eng. 2001;13:136-42.

[19] Ryou JS, Otsuki N. Experimental study on repair of concrete structural members by electrochemical method. Scripta Mater. 2005;52:1123-7.

[20] Ryu JS. Influence of crack width, cover depth, water-cement ratio and temperature on the formation of electrodeposits on the concrete surface. Magazine of Concrete Research. 2003;55:35-40.

[21] Xia J, Cheng X, Liu QF, Xie HB, Zhong XP, Jin SJ, et al. Effect of the stirrup on the transport of chloride ions during electrochemical chloride removal in concrete structures. Constr Build Mater. 2020;250.

[22] Yeih W, Chang JJ, Chang CC, Chen KL, Chi MC. Electrochemical chloride removal for reinforced concrete with steel rebar cage using auxiliary electrodes. Cement Concrete Comp. 2016;74:136-46.

[23] Xu JX, Shan HY, Zhang CK, Jiang LH, Tang L, Xu Y, et al. Surface coating treatment and densification of mortar by electrodeposition method. Magazine of Concrete Research. 2016;68:69-79.

[24] Xia J, Li LY. Numerical simulation of ionic transport in cement paste under the action of externally applied electric field. Constr Build Mater. 2013;39:51-9.

[25] Liu QF, Easterbrook D, Yang J, Li LY. A three-phase, multi-component ionic transport model for simulation of chloride penetration in concrete. Eng Struct. 2015;86:122-33.

[26] Liu QF, Li LY, Easterbrook D, Yang J. Multi-phase modelling of ionic transport in concrete when subjected to an externally applied electric field. Eng Struct. 2012;42:201-13.

[27] Bai Y, Wang Y, Xi YP. Modeling the effect of temperature gradient on moisture and ionic transport in concrete. Cement Concrete Comp. 2020;106.

[28] Liu QF, Yang J, Xia J, Easterbrook D, Li LY, Lu XY. A numerical study on chloride migration in cracked concrete using multi-component ionic transport models. Comp Mater Sci. 2015;99:396-416.

[29] Yang P, Sant G, Neithalath N. A refined, self-consistent Poisson-Nernst-Planck (PNP) model for electrically induced transport of multiple ionic species through concrete. Cement Concrete Comp. 2017;82:80-94.

[30] Mao LX, Hu Z, Xia J, Feng GL, Azim I, Yang J, et al. Multi-phase modelling of electrochemical rehabilitation for ASR and chloride affected concrete composites. Compos Struct. 2019;207:176-89.

[31] Dunant CF, Scrivener KL. Physically based models to study the alkali-silica reaction. Proc Inst Civ Eng-Co. 2016;169:136-44.

[32] Savija B, Lukovic M, Pacheco J, Schlangen E. Cracking of the concrete cover due to reinforcement corrosion: A two-dimensional lattice model study. Constr Build Mater. 2013;44:626-38.

[33] Thilakarathna PSM, Baduge KSK, Mendis P, Vimonsatit V, Lee H. Mesoscale modelling of concrete - A review of geometry generation, placing algorithms, constitutive relations and applications. Eng Fract Mech. 2020;231.

[34] Trawinski W, Tejchman J, Bobinski J. A three-dimensional meso-scale modelling of concrete fracture, based on cohesive elements and X-ray mu CT images. Eng Fract Mech. 2018;189:27-50.

[35] Wang Y, Jiradilok P, Nagai K, Asamoto S. A mesoscale discrete model for mechanical performance of concrete damaged by coupled ASR and DEF. Eng Fract Mech. 2020;232.

[36] Wang Y, Meng YS, Jiradilok P, Matsumoto K, Nagai K, Asamoto S. Expansive cracking and compressive failure simulations of ASR and DEF damaged concrete using a mesoscale discrete model. Cement Concrete Comp. 2019;104.

[37] Miura T, Multon S, Kawabata Y. Influence of the distribution of expansive sites in aggregates on microscopic damage caused by alkali-silica reaction: Insights into the mechanical origin of expansion. Cement Concrete Res. 2021;142.

[38] Pan JW, Xu YJ, Jin F, Zhang CH. A unified approach for long-term behavior and seismic

response of AAR-affected concrete dams. Soil Dyn Earthq Eng. 2014;63:193-202.

[39] Pan J, Xu Y, Jin F, Zhang C. Modeling of long-term behavior of concrete dams affected by alkali-aggregate reaction. Shuili Fadian Xuebao/Journal of Hydroelectric Engineering. 2014;33:169-76.

[40] Dunant C. Experimental and modelling study of the alkali-silica-reaction in concrete. EPFL; 2009.

[41] Giorla AB, Scrivener KL, Dunant CF. Influence of visco-elasticity on the stress development induced by alkali-silica reaction. Cement Concrete Res. 2015;70:1-8.

[42] Multon S, Sellier A. Expansion modelling based on cracking induced by the formation of new phases in concrete. Int J Solids Struct. 2019;160:293-306.

[43] Ryu JS, Otsuki N. Crack closure of reinforced concrete by electrodeposition technique. Cement Concrete Res. 2002;32:159-64.

[44] Nishida T, Otsuki N, Saito A. Development of Improved Electrodeposition Method for Repair of Reinforced Concrete Structures. 2014.

[45] Chu HQ, Jiang LH, Song ZJ, Xu Y, Zhao SJ, Xiong CS. Repair of concrete crack by pulse electro-deposition technique. Constr Build Mater. 2017;148:241-8.

[46] Chu HQ, Jiang LH, Xiong CS, You LS, Xu N. Use of electrochemical method for repair of concrete cracks. Constr Build Mater. 2014;73:58-66.

[47] Chu HQ, Liang YC, Guo MZ, Zhu ZY, Zhao SJ, Song ZJ, et al. Effect of electro-deposition on repair of cracks in reinforced concrete. Constr Build Mater. 2020;238.

[48] Chen Q, Jiang ZW, Zhu HH, Ju JW, Yan ZG, Li HX, et al. A multiphase micromechanical model for unsaturated concrete repaired by electrochemical deposition method with the bonding effects. Int J Damage Mech. 2018;27:1307-24.

[49] Chen Q, Jiang ZW, Yang ZH, Zhu HH, Ju JW, Yan ZG, et al. Differential-scheme based micromechanical framework for unsaturated concrete repaired by the electrochemical deposition method. Acta Mech. 2017;228:415-31.

[50] Zhou YT, Liu W, Chen Q, Li HX, Zhu HH, Ju JW. Multiphysics coupling model for the crack repairing process using electrochemical deposition. Constr Build Mater. 2020;264.

[51] Multon S, Sellier A, Cyr M. Chemo-mechanical modeling for prediction of alkali silica

reaction (ASR) expansion. Cement Concrete Res. 2009;39:490-500.

[52] Luping T, Nilsson L-O. Chloride binding capacity and binding isotherms of OPC pastes and mortars. Cement Concrete Res. 1993;23:247-53.

[53] Sergi G, Yu S, Page C. Diffusion of chloride and hydroxyl ions in cementitious materials exposed to a saline environment. Magazine of Concrete Research. 1992;44:63-9.

[54] Kim T, Olek J, Jeong H. Alkali-silica reaction: Kinetics of chemistry of pore solution and calcium hydroxide content in cementitious system. Cement Concrete Res. 2015;71:36-45.

[55] Savija B, Liu D, Smith G, Hallam KR, Schlangen E, Flewitt PEJ. Experimentally informed multi-scale modelling of mechanical properties of quasi-brittle nuclear graphite. Eng Fract Mech. 2016;153:360-77.

[56] Bazant ZP, Yu Q. Size-Effect Testing of Cohesive Fracture Parameters and Nonuniqueness of Work-of-Fracture Method. J Eng Mech. 2011;137:580-8.

[57] Sun W, Liu GC, Wang LD, Wu TT, Liu Y. An arbitrary Lagrangian-Eulerian model for studying the influences of corrosion product deposition on bimetallic corrosion. J Solid State Electr. 2013;17:829-40.

[58] Xiao JZ, Ying JW, Shen LM. FEM simulation of chloride diffusion in modeled recycled aggregate concrete. Constr Build Mater. 2012;29:12-23.

[59] Gao Y, De Schutter G, Ye G, Tan ZJ, Wu K. The ITZ microstructure, thickness and porosity in blended cementitious composite: Effects of curing age, water to binder ratio and aggregate content. Compos Part B-Eng. 2014;60:1-13.

[60] Zhang HZ, Savija B, Schlangen E. Combined experimental and numerical study on micro-cube indentation splitting test of cement paste. Eng Fract Mech. 2018;199:773-86.

[61] Cheng X, Xia J, Wang WL, Jin SJ, Huang N, Jin WL. Numerical modeling of the effect of concrete porosity evolution on electrochemical chloride removal from concrete structures. Constr Build Mater. 2021;267.

[62] Trawinski W, Bobinski J, Tejchman J. Two-dimensional simulations of concrete fracture at aggregate level with cohesive elements based on X-ray mu CT images. Eng Fract Mech. 2016;168:204-26.

[63] Jin L, Xu JD, Zhang RB, Du XL. Numerical study on the impact performances of

reinforced concrete beams: A mesoscopic simulation method. Eng Fail Anal. 2017;80:141-63.

[64] Djerbi A, Bonnet S, Khelidj A, Baroghel-Bouny V. Influence of traversing crack on chloride diffusion into concrete. Cement Concrete Res. 2008;38:877-83.

[65] Zou DJ, Qin SS, Liu TJ, Jivkov A. Experimental and numerical study of the effects of solution concentration and temperature on concrete under external sulfate attack. Cement Concrete Res. 2021;139.

[66] Ulm FJ, Coussy O, Li KF, Larive C. Thermo-chemo-mechanics of ASR expansion in concrete structures. J Eng Mech. 2000;126:233-42.

[67] Larive C. Apports combinés de l'expérimentation et de la modélisation à la compréhension de l'alcali-réaction et de ses effets mécaniques: Ecole nationale des ponts et chaussees; 1997.

[68] Kawabata Y, Seignol JF, Martin RP, Toutlemonde F. Macroscopic chemo-mechanical modeling of alkali-silica reaction of concrete under stresses. Constr Build Mater. 2017;137:234-45.

[69] Pan JW, Feng YT, Jin F, Xu YJ, Sun QC, Zhang CH, et al. Meso-scale particle modeling of concrete deterioration caused by alkali-aggregate reaction. Int J Numer Anal Met. 2013;37:2690-705.

[70] Fang YP, Du KQ, Guo QZ, Feng QP, Li DY, Wang C. Investigation of electrochemical chloride removal from concrete using direct and pulse current. Constr Build Mater. 2021;270.

[71] Liu QF, Xia J, Easterbrook D, Yang J, Li LY. Three-phase modelling of electrochemical chloride removal from corroded steel-reinforced concrete. Constr Build Mater. 2014;70:410-27.